Chapter 4

Four-wave mixing in PCF's and tapered fibers

The dramatically increased nonlinear response in PCF's in combination with single-mode behavior over almost the entire transmission range and the engineerable dispersion characteristic suggest that new phenomena could appear also in other nonlinear processes. In particular four-wave mixing (FWM) is one of such processes which should be possible in a much wider frequency range than in standard fibers, and is promising for applications.

The third-order nonlinear polarization leads in general to the interaction of four optical waves with frequencies $\omega_1, \omega_2, \omega_3, \omega_4$ and include such phenomena as FWM and parametric amplification. These processes can be used to generate waves at new frequencies. In the degenerate case $\omega_1 = \omega_2 = \omega_P$ two photons of a strong pump pulse are annihilated with simultaneous creation of two photons at $\omega_S = \omega_P + \Omega$ and $\omega_I = \omega_P - \Omega$. This process can be analitycally described for the case when the pulse durations are long enough so that effects of linear dispersion are negligible, the pump pulse is much

stronger than sideband beams, the depletion of pump can be neglected, and the loss is absent. In this case the description of the process is given by [50]

$$\frac{\partial A_{S,I}}{\partial \xi} = 2i\gamma_{S,I}|A_P|^2 A_{S,I} + i\gamma_{S,I} A^*_{I,S} A_p^2 \exp(-i\Delta k_0 z) \quad (4.1)$$

$$\frac{\partial A_P}{\partial \xi} = i\gamma_P |A_P|^2 A_P, \quad (4.2)$$

where $A_{P,S,I}$ are the envelopes of pump, signal, and idler, respectively, $\gamma_{P,S,I} = \omega_{P,S,I} n_2/(cA_{eff})$, A_{eff} is the effective nonlinear mode area which is assumed to be the same for all pulses, and $\Delta k_0 = \beta(\omega_S) + \beta(\omega_I) - 2\beta(\omega_P)$. The pump field is found in the form $A_P = A_{P0}\exp(i\gamma_P|A_{P0}|^2\xi)$, and for the the sidebands the substitution $A_{S,I} = \tilde{A}_{S,I}\exp(i2\gamma_{S,I}|A_{P0}|^2\xi)$ reduces the original system to

$$\frac{\partial \tilde{A}_{S,I}}{\partial \xi} = \gamma_{S,I}\tilde{A}^*_{I,S}|A_{P0}|^2 \exp(2i\gamma_P - i\Delta k_0 \xi) \quad (4.3)$$

which has solutions in the form of waves growing as $\exp(g\xi)$ with

$$g = \sqrt{(\gamma_P P_0)^2 - (\Delta k_0 + 2\gamma_P P_0)^2}. \quad (4.4)$$

Maximum gain $g_{max} = \gamma_P P_0$ occurs if the phase-matching condition $\Delta k_0 + 2\gamma_P P_0 = 0$ is satisfied.

4.1 Phase-matching condition

In collinear propagation as in fibers significant FWM occurs only if the phase-matching relation [50] $\Delta k = \Delta k_M + \Delta k_{WG} + \Delta k_{NL} = 0$ is nearly satisfied. Here $\Delta k_M, \Delta_{WG}, \Delta k_{NL} = 2W n_2 \omega_p I_p/c$ represent the wavevector mismatch occurring as a result of material dispersion, waveguide dispersion and the nonlinear contribution to the refractive index, respectively. For standard optical fibers FWM has been studied extensively [50]. Phase matching can

be achieved in multimode fibers by using different modes or in birefringent fibers by the different effective index for waves propagating with orthogonal polarization. In single-mode nonbirefringent fibers phase matching can be satisfied near the zero-dispersion wavelength around 1.28 μm for very specific conditions for the pump frequency because the material contribution becomes quite small and can be compensated by the waveguide contribution. When the pump wavelength lies in the anomalous dispersion region the negative material and waveguide contribution can be compensated by the positive nonlinear contribution. In both cases the frequency shift is typically lower than 100 THz. At visible frequencies of the pump wave, FWM has been demonstrated in weakly birefringent single-mode fibers [88]. In a nonbirefringent single-mode fiber phase matching has been achieved in the visible range by a combination of SPM and cross-phase modulation [89]. Recently FWM has been observed in microstructure fibers in the optical region at 753 nm with a frequency shift of about 100 THz [15].

To study FWM in PCF's or tapered fibers, first we consider the phase matching condition. In Fig. 4.1 the wave vector mismatch

$$\Delta k_m + \Delta k_{WG} = \beta(\omega_s)\omega_s + \beta(\omega_I)\omega_I - 2\beta(\omega_p)\omega_p \tag{4.5}$$

is presented. Here $\beta(\omega)$ is the eigenvalue of the Helmholtz equation including both the waveguide and the material contribution which was found numerically as described in Chapter 2. Phasematched idler and signal frequencies can be found as common points of the horizontal line drawn at the pump intensity and the curve corresponding to the pump frequency. As can be seen, phasematching in a PCF shows a rather distinct behavior from standard fibers (compare [50]) caused by the large waveguide contribution Δk_{WG}

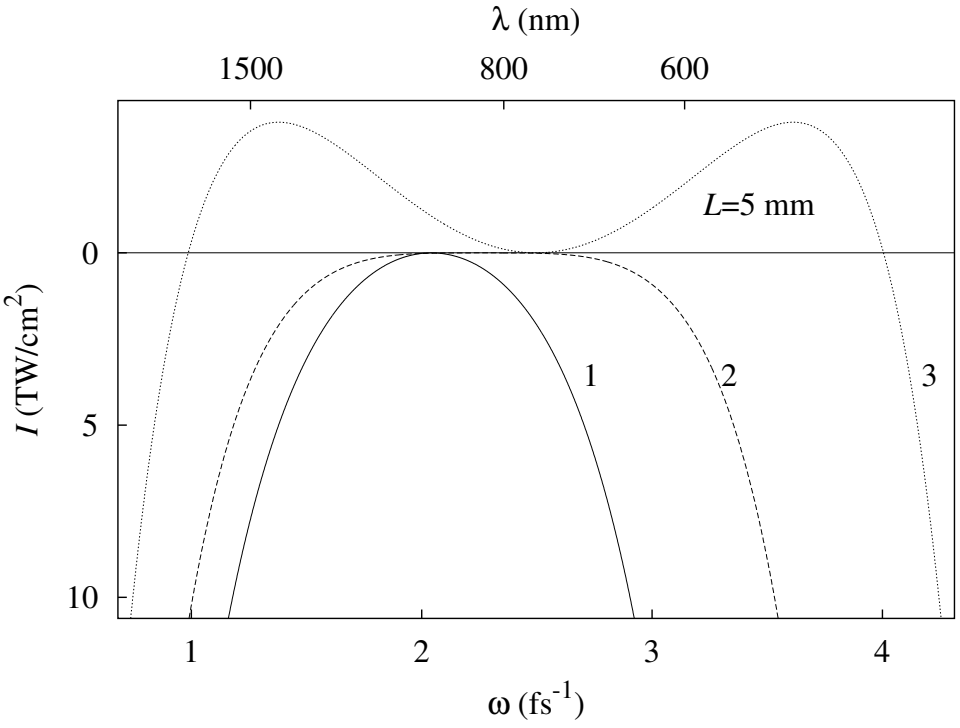

Figure 4.1: Phase-matching for 2.95-μm-diameter tapered fiber and different input frequencies: $0.9\omega_0$ (curve 1), $1.0\omega_0$ (curve 2), $1.1\omega_0$ (curve 3) with ω_0 =2.27 fs^{-1}. Phase-matched frequencies are determined as crossing points of the corresponding curve and the horizontal line at $I = I_P$.

to the wavevector mismatch. In Fig. 4.1, the PCF with large hole radius (or tapered fiber) with parameters as given in the caption and a zero-dispersion wavelength of 830 nm (for three different pump frequencies) is considered. All considered pump frequencies are within the tuning range of a Ti:sapphire laser. As can be seen the possible frequency shifts to the idler and the signal waves are now in the range of the pump carrier frequency and more than one order of magnitude larger than in standard fibers. In particular for the input frequency of 2.5 fs^{-1} the idler wavelength is about 1600 nm and the signal at 400 nm. Small changes of the pump frequency lead to a huge range of detuning covering the range of IR up to the blue. Since additionally the geometry parameters of the PCF can be adjusted during the fabrication process, WFM in PCF's offers the potential for the use of broadband parametric amplifiers, frequency shifters and other interesting devices.

4.2 Competition with supercontinuum generation by soliton fission.

We start the numerical study of FWM by examining the propagation of a 200-fs-long pulse with $I_0 = 2.0$ TW/cm^2 in a 2.95-μm-thick tapered fiber or in a PCF structure with very thin silica bridges [cf Fig. 1.1]. The propagation is described by the forward Maxwell equation (2.66). The input central frequency $\omega_0 = 2.27$ fs^{-1} coincides with the zero-dispersion frequency of this fiber. The evolution of the pulse shapes and spectra are illustrated in Fig. 4.2(a) and Fig. 4.2(b). During the initial stage of propagation, SPM causes slight broadening of the spectrum around the input frequency. With longer

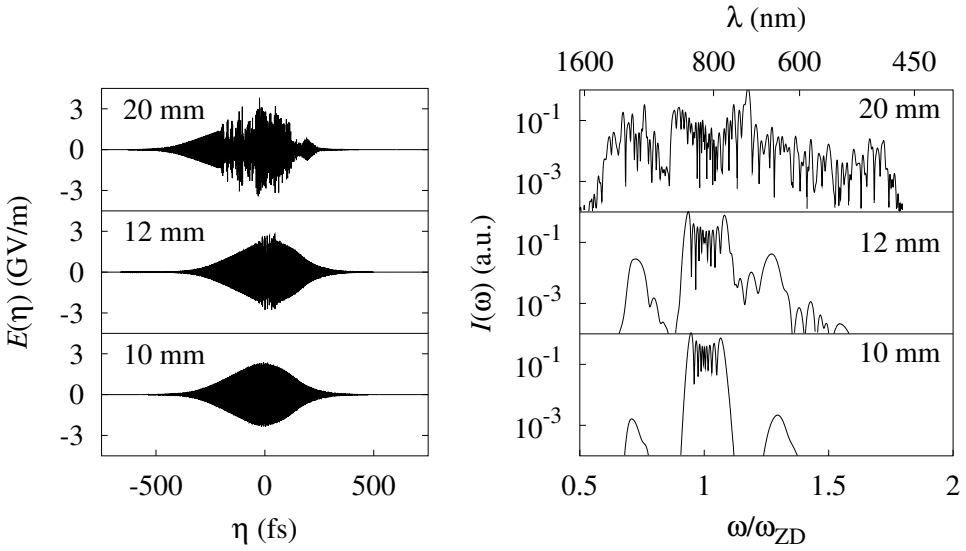

Figure 4.2: Evolution of output pulse shape (a) and spectrum (b) for $\omega_0 = \omega_{ZD}$, I_0=2 TW/cm^2, τ_0=200 fs in 2.95-μm-diameter tapered fiber.

propagation length, two additional peaks arise at wavelengths $\sim$ 1150 nm and 640 nm, which agree rather well with those predicted by the phase-matching condition in Fig. 4.1. At around 12 mm propagation length, seen in the middle section of Fig. 4.2, additional spectral components are generated. The temporal shape shows in the central part besides fast oscillating also low oscillating components, arising from the superposition of the different side peaks in the spectrum seen on the left side. With longer propagation to 20 mm the part of radiation transferred to the anomalous dispersion region by FWM and SPM is sufficient to form solitons. As can be seen in the upper section now a wide-band SC reaching from 500 nm to 1600 nm is generated and several peaks arise in the temporal shape. With further propagation these peaks move with different velocities and form separated pulses which do not change their form during further propagation (not shown here). This

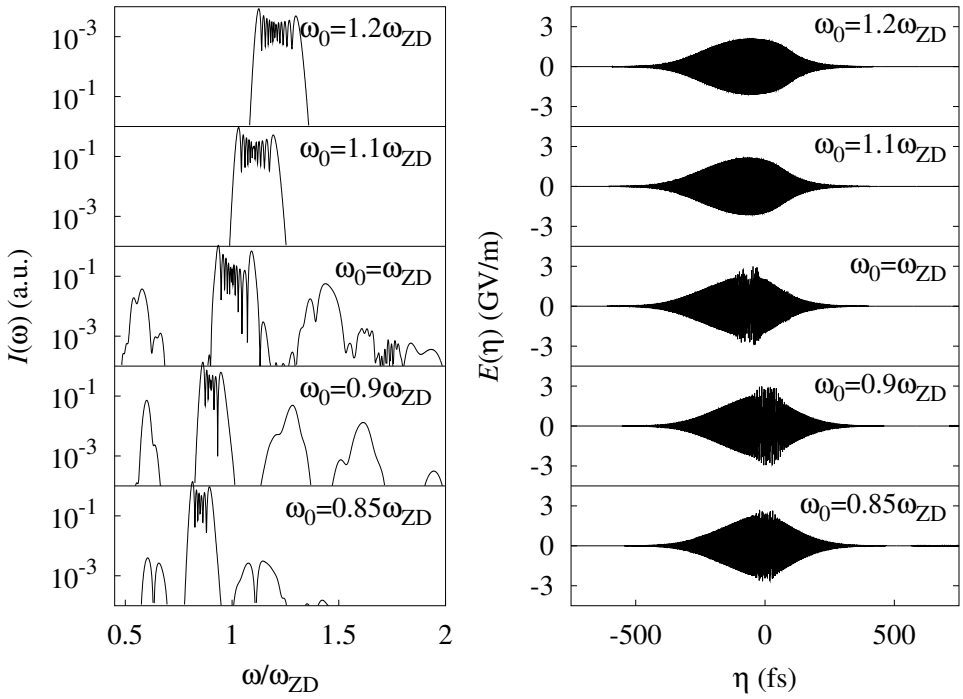

Figure 4.3: Output spectra (a) and pulse shapes (b) for L=3 mm, I_0=8.7 TW/cm^2, τ_0=200 fs and different input frequencies as indicated.

allows the interpretation that the SC in the upper part of Fig. 4.2 is caused by fission of higher-order solitons as described in Chapter 3. However, FWM and SPM is the dominant process on the early stages of propagation, which is responsible for generating new frequency components.

As discussed above and seen in Fig. 4.1 the dispersion properties of the medium have a large influence on the 4-wave-mixing processes. In Fig. 4.3, we compare the spectra of pulses with different input frequencies in anomalous ($\omega_0 < \omega_{ZD}$) and normal ($\omega_0 > \omega_{ZD}$) dispersion regions but for the same intensity $I_0 = 8.7$ TW/cm^2 and pulse duration $\tau_0 = 200$ fs with fiber length $L = 3$ mm. In the anomalous dispersion regime, similar to the previous case new spectral components arise on both sides of the input peak. As predicted

by comparison of curves 1 and 2 in Fig. 4.1, the frequency difference to the side peak is larger for the frequencies closer to the zero-dispersion point. This allows to control the wavelength of the generated radiation by a slight shift of the input frequency. For $\omega_0 = 0.9\omega_{ZD}$ an additional spectral peak on the blue side is seen. This peak is generated by cascaded 4-wave mixing. However, for frequencies in the normal dispersion region, no side peaks caused by FWM are generated and only spectral broadening by SPM can be seen. The temporal shapes for the input frequencies in the anomalous dispersion region and at the zero-dispersion frequency show low and high-frequency components as expected from the spectrum, in contrast to the shapes for $\omega_0 > \omega_{ZD}$ where the low-frequency components do not arise. With further propagation, as illustrated by Fig. 4.4, for $\omega_0 < \omega_{ZD}$ a significant part of the spectrum is in the anomalous dispersion region. This part forms a higher-order soliton, its fission leads to the generation of a SC covering more than 1 octave from 600 to 1400 nm as described in the previous chapter. The separate peaks in the temporal shape are identified as solitons, while the trailing part of the pulses consists of NSR. For $\omega_0 = 1.1\omega_{ZD}$, broadening by SPM also induces spectral components in the anomalous dispersion regime which also forms a higher-order soliton. After its fission a SC is generated which is now narrower than in the previous cases. The above given interpretation is supported by the evolution of the spectra for higher input frequencies in the normal dispersion region. As can be seen in Fig. 4.4 for $\omega_0 = 1.2\omega_{ZD}$ after 10 mm of propagation a spectrum arises that is remarkably narrower than for lower input frequencies and shows the typical behavior of SPM-induced spectral broadening. The generated spectral components are here too far from the zero-dispersion point and therefore no solitons can be formed in the anoma-

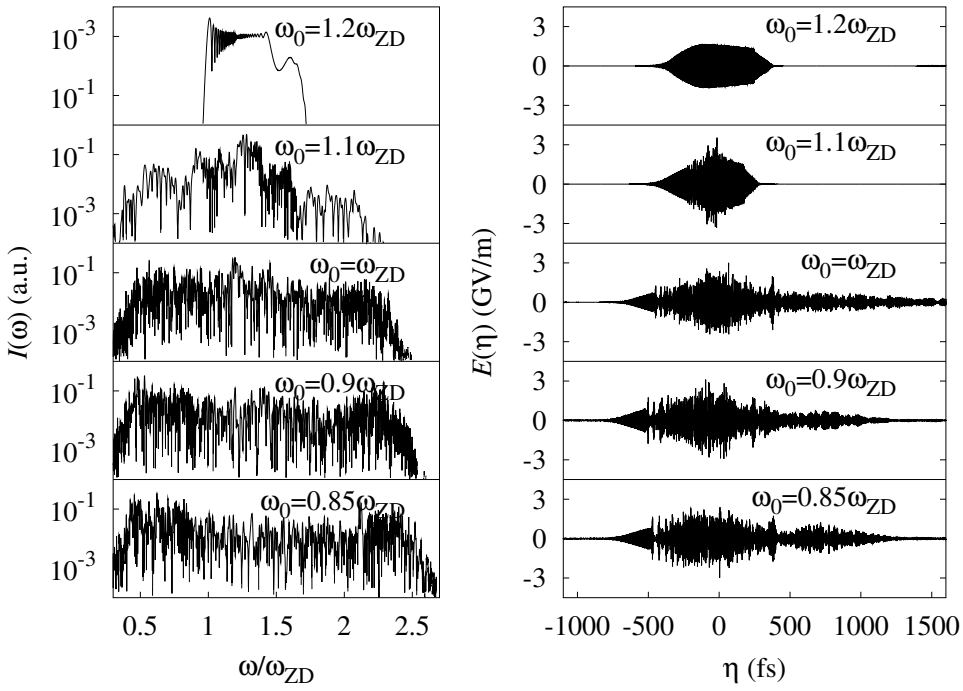

Figure 4.4: Output spectra (a) and pulse shapes (b) for L=10 mm, I_0=8.7 TW/cm^2, τ_0=200 fs and different input frequencies as indicated.

lous region. Therefore, the final spectrum qualitatively differ from the other cases because fission of higher-order solitons does not occur. The temporal shape in this case does not show spikes but only a temporal elongated smooth pulse which is typical for SPM in the normal dispersion region.

Finally we study the possibility of generating pulses further in the IR by means of 4-wave mixing. As shown in Fig. 4.5(a), after propagation of 1 mm in a 2.95-μm-diameter tapered fiber radiation is generated as a separate peak around $\sim$2000 nm. The FWHM duration of this radiation is 140 fs. A higher intensity of 27 TW/cm^2 is necessary in this case. Note that with further propagation SC will be generated. Therefore it is important that the fiber length be chosen correctly. Thus 4-wave mixing can be used for producing spectrally-separated radiation at around 2000 nm. Additionally, we study the possibility to enhance 4-wave mixing by sending two pulses of the same intensity 12.4 TW/cm^2 at frequencies of $1.1\omega_{ZD}$ and $1.85\omega_{ZD}$ which are chosen to be phasematched. As one can see in Fig. 4.5(b), the generated radiation does not move further in the IR and is not significantly stronger, and moreover it reveals a slightly irregular spectral shape.

4.3 Four-wave mixing for very low intensity and long pulses

Four-wave mixing with large $\Delta\omega$ [16] has important applications, for example in WDM systems, and therefore deserve a separate study. As it was shown in the previous sections, for shorter pulse duration due to walk-off the effective FWM is difficult to achieve for the most interesting regime with pump in

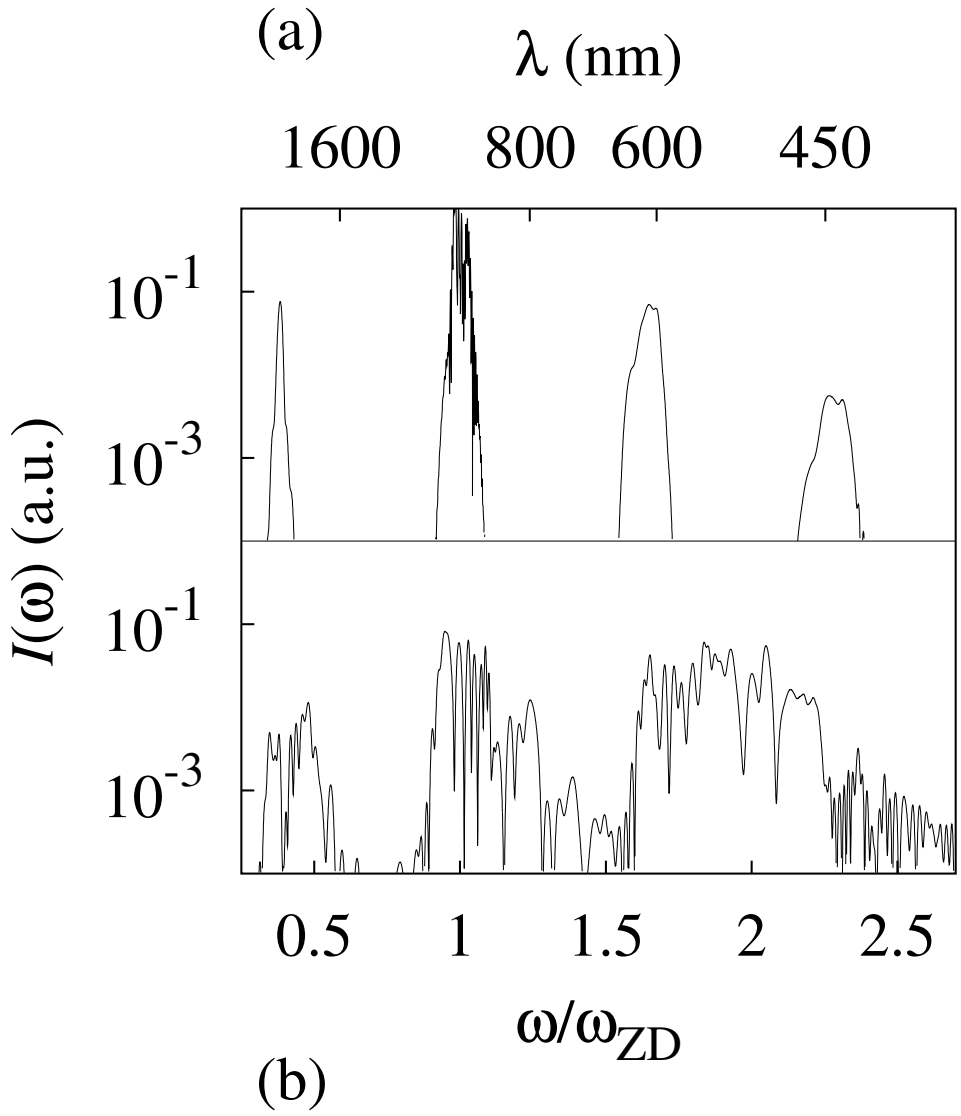

Figure 4.5: Output spectra for L=1 mm and (a) I_0=27 TW/cm^2, τ_0=200 fs,$\omega_0 = \omega_{ZD}$; (b) two pulses with $I_{0,1} = I_{0,2} = 12.4$ TW/cm^2, $\tau_{0,1} = \tau_{0,2} = 100$ fs, $\omega_{0,1} = 1.1\omega_{ZD}$, $\omega_{0,2} = 1.84\omega_{ZD}$.

the anomalous region. Therefore, here we study this process for longer ns-duration pulses and much smaller intensity. For such pulses, methods which imply the resolution of carrier oscillations are no longer necessary and are in fact not applicable due to the large time window. Therefore these processes can be studied by standard slowly varying envelope approximation equations (2.24). The main definitions are repeated here for sake of completeness. The electric field propagating in the z direction is represented as $\vec{E}_x(z,t) = \exp[i(\omega_x t - \beta_x z)]\vec{F}(\vec{r}_\perp,\omega_x)A(z,\eta)$, where ω_x is the carrier frequency, the index $x = \mathrm{P,I,S}$ denotes pump, idler, and signal wave, respectively. The function $\vec{F}(\vec{r}_\perp,\omega_x)$ is the transverse distribution of the field in the cross-section S of the fiber, $\beta(\omega)$ is the wavevector and $A(z,\eta)$ is the slowly-varying envelope with $\eta = t - z/v_{g,\mathrm{P}}$. The group velocity $v_{g,x}$ is given by $v_{g,x} = [d\beta/d\omega(\omega_x)]^{-1}$. We use the standard propagation equation to describe the evolution of $A(\xi,\eta)$ [50]:

$$\begin{aligned}
\frac{\partial A_\mathrm{P}}{\partial z} &= A_\mathrm{P}\left(-\alpha + i\gamma_\mathrm{P}[|A_\mathrm{P}|^2 + 2|A_\mathrm{I}|^2 + 2|A_\mathrm{S}|^2]\right) \\
&+ 2i\gamma_\mathrm{P}A_\mathrm{P}^* A_\mathrm{S} A_\mathrm{I}\exp(i\Delta_k z) + i\beta''(\omega_P)\frac{\partial^2 A_\mathrm{P}}{\partial\eta^2} \\
\frac{\partial A_\mathrm{S}}{\partial z} &= A_\mathrm{S}\left(-\alpha + i\gamma_\mathrm{S}[|A_\mathrm{S}|^2 + 2|A_\mathrm{P}|^2 + 2|A_\mathrm{I}|^2]\right) \\
&+ i\gamma_\mathrm{S}A_\mathrm{I}^* A_\mathrm{P}^2\exp(-i\Delta_k z) + \left(\frac{1}{v_{g,\mathrm{P}}} - \frac{1}{v_{g,\mathrm{S}}}\right)\frac{\partial A_\mathrm{S}}{\partial\eta} + i\beta''(\omega_S)\frac{\partial^2 A_\mathrm{S}}{\partial\eta^2} \\
\frac{\partial A_\mathrm{I}}{\partial z} &= A_\mathrm{I}\left(-\alpha + i\gamma_\mathrm{I}[|A_\mathrm{I}|^2 + 2|A_\mathrm{S}|^2 + 2|A_\mathrm{P}|^2]\right) \\
&+ i\gamma_\mathrm{I}A_\mathrm{S}^* A_\mathrm{P}^2\exp(-i\Delta_k z) + \left(\frac{1}{v_{g,\mathrm{P}}} - \frac{1}{v_{g,\mathrm{I}}}\right)\frac{\partial A_\mathrm{I}}{\partial\eta} + i\beta''(\omega_I)\frac{\partial^2 A_\mathrm{I}}{\partial\eta^2} \quad (4.6)
\end{aligned}$$

In these equations $\gamma_x = n_2\omega_x/(cA_{eff})$, n_2 is the nonlinear refractive index, α is the loss, $A_{eff} = (\int_S F(\vec{r}_\perp)^2 dS)^2/\int_S F^4(\vec{r}_\perp)dS$ is the effective nonlinear area of the mode which was assumed to be equal for all three waves, $\beta'' = d^2\beta/d\omega^2$. Higher-order nonlinear effects, the Raman effect and higher-order dispersion

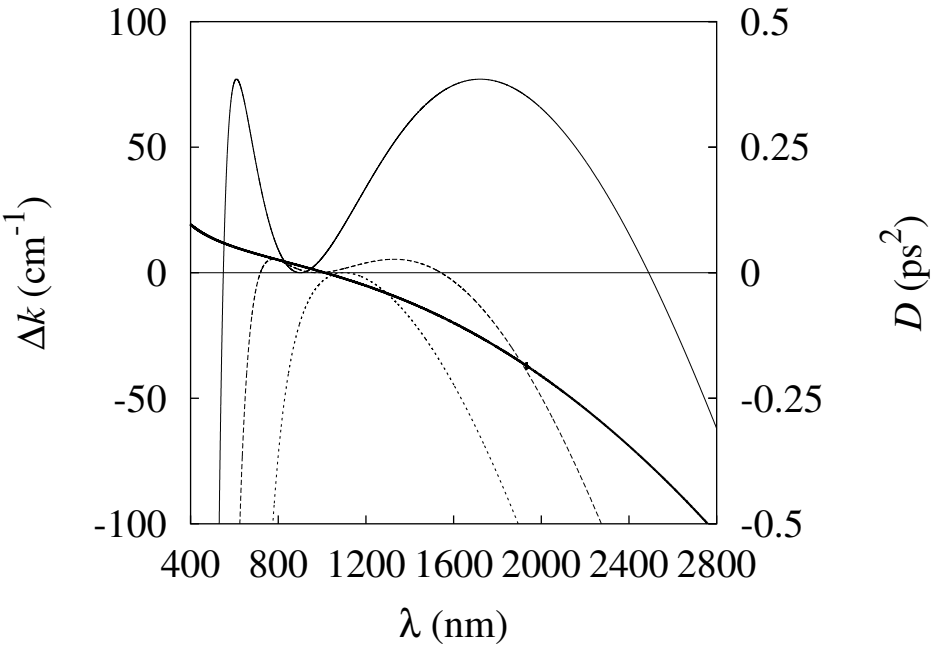

Figure 4.6: Dispersion coefficient D (thick solid curve) and phase mismatch for pump wavelengths of 1100 nm (dotted curve), 980 nm (dashed curve) and 900 nm (thin solid curve) as a function of the idler wavelength. PCF parameters are $\Lambda = 3.5$ μm, $d = 2.5$ μm.

effects were neglected, which is valid for low-intensity pulses with nanosecond duration considered here.

4.3.1 Phase matching in dependence on fiber geometry

First we consider the phase matching in a photonic crystal fiber with $\Lambda = 3.5$ μm and $d = 2.5$ μm for pump wavelengths of 900, 980 and 1100 nm as presented by thin curves in Fig. 4.6. The dispersion coefficient $D = L\beta''(\lambda)$ is shown by a thick line for $L = 1$ m fiber length. No phase-matching is achieved for λ_p=1100 nm, since this wavelength is in the anomalous dispersion range,

above the zero-dispersion wavelength $\lambda_{ZD} = 1013$ nm, and $-12\beta''/\beta^{(4)} < 0$. For $\lambda_P = 980$ nm, β'' changes the sign and therefore phase matching with large distance to the sidebands is achieved. Note that this situation is opposite to that for standard telecommunication fibers, for which phase matching can occur with the pump wavelength in the anomalous dispersion regime. In contrast, in PCF's effective FWM is possible with λ_P in the near-infrared and visible region, which means that many easily available sources can be used to generate the pump wave. With further shift of the λ_P to the visible, the spectral distance to the sidebands increases. However, losses in the far-IR region soon overweigh the gain and no effective FWM is possible for shorter pump wavelengths with the chosen PCF parameters.

Since dispersion properties have a crucial effect on the FWM in the photonic fiber, we now examine the dependence of the idler and signal wavelengths on the geometry of the fiber. In Fig. 4.7, the dependence of these wavelengths versus the hole diameter for fibers with $\Lambda = 3.5$ μm is presented for two pump wavelengths λ_P of 980 and 1100 nm. As soon as the zero-dispersion wavelength becomes larger than the λ_P, solutions of phase-matching conditions arise. For $\lambda_P \simeq \lambda_{ZD}$, the approximate relation for $\omega_{S,I}$ derived earlier in the text can be modified to describe the dependence of phase-matched wavelengths on d:

$$\lambda_{S,I} = \lambda_P \left(1 \pm \sqrt{\frac{12\beta'''(d_{ZD} - d)\partial\omega_{ZD}/\partial d}{\beta^{(4)}}} \right)^{-1}, \qquad (4.7)$$

where $\omega_{ZD}(d_{ZD}) = \omega_P$. This approximation (shown by dashed lines in Fig. 4.7) satisfactorily corresponds to the results of the numerical calculation in the region λ_P.

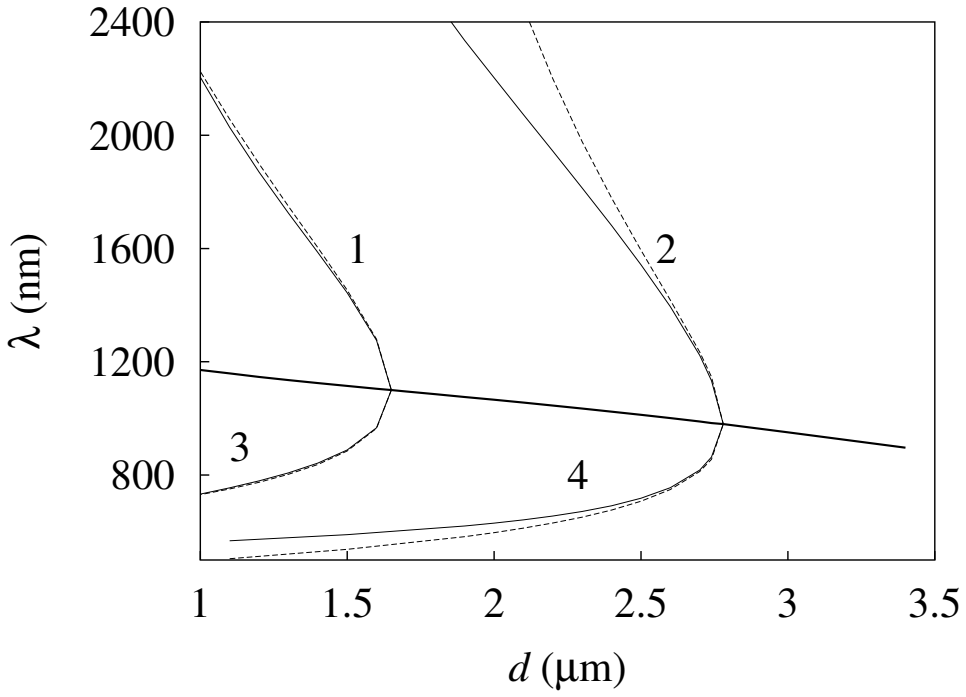

Figure 4.7: Dependence of zero-dispersion wavelength, idler wavelength, and signal wavelength on the hole diameter d for PCF with $\Lambda = 3.5$ μm. Idler (curves 1 and 2) and signal (curves 3 and 4) wavelengths are shown for pump wavelength of 1100 nm (curves 1 and 3) and 980 nm (curves 2 and 4). The zero-dispersion wavelength is shown by the thick solid line, dotted lines represent approximate estimates (4.7).

4.3.2 Numerical results

To examine the temporal and spectral evolution of the light generated by FWM, we numerically solve the system (4.6) for PCF with $\Lambda = 3.5$ μm, $d = 3.4$ μm and input pump pulse with $\lambda_P = 875$ nm, FWHM duration of 0.6 ns and two different peak intensities of 5.4×10^8 W/cm^2 and 1.8×10^9 W/cm^2. The input signal has ten orders of magnitude lower intensity, the loss $\alpha = 0.02m^{-1}$ is included phenomenologically. As can be seen from the results for lower intensity presented in Fig. 4.8(a),(c),(e), during propagation up to 25 m the idler pulse experiences gain of $\sim$26 dB (for field), which corresponds very good to both the theoretical prediction of 25.5 dB and the experimental results obtained for similar fiber and input pulse parameters in Ref. [15]. For larger propagation length, due to walk-off effects and decreasing pump intensity due to loss, the phase-matching condition is no longer satisfied which drastically reduces the gain. The idler pulse is not noticeably amplified during the next 25 m of propagation (see Fig. 4.8). Its intensity remains around 5 orders of magnitude lower than that of the pump pulse. Note that the generated radiation remains spectrally narrow, with maximum width not exceeding 0.2 nm. The situation significantly changes for higher input pump intensity, as illustrated in Fig. 4.8(b),(d),(f). The energy transfer from the pump to the idler and the signal waves is strong enough to amplify the latter pulses to the intensity level of pump. Similar to the lower-intense case, propagation further than 25 m does not amplify the idler pulse any more due to losses and pump depletion seen as irregularities in the pump temporal profile in Fig. 4.8(f). In contrast to the previous case, the spectrum of the idler pulse is significantly broader, which we attribute

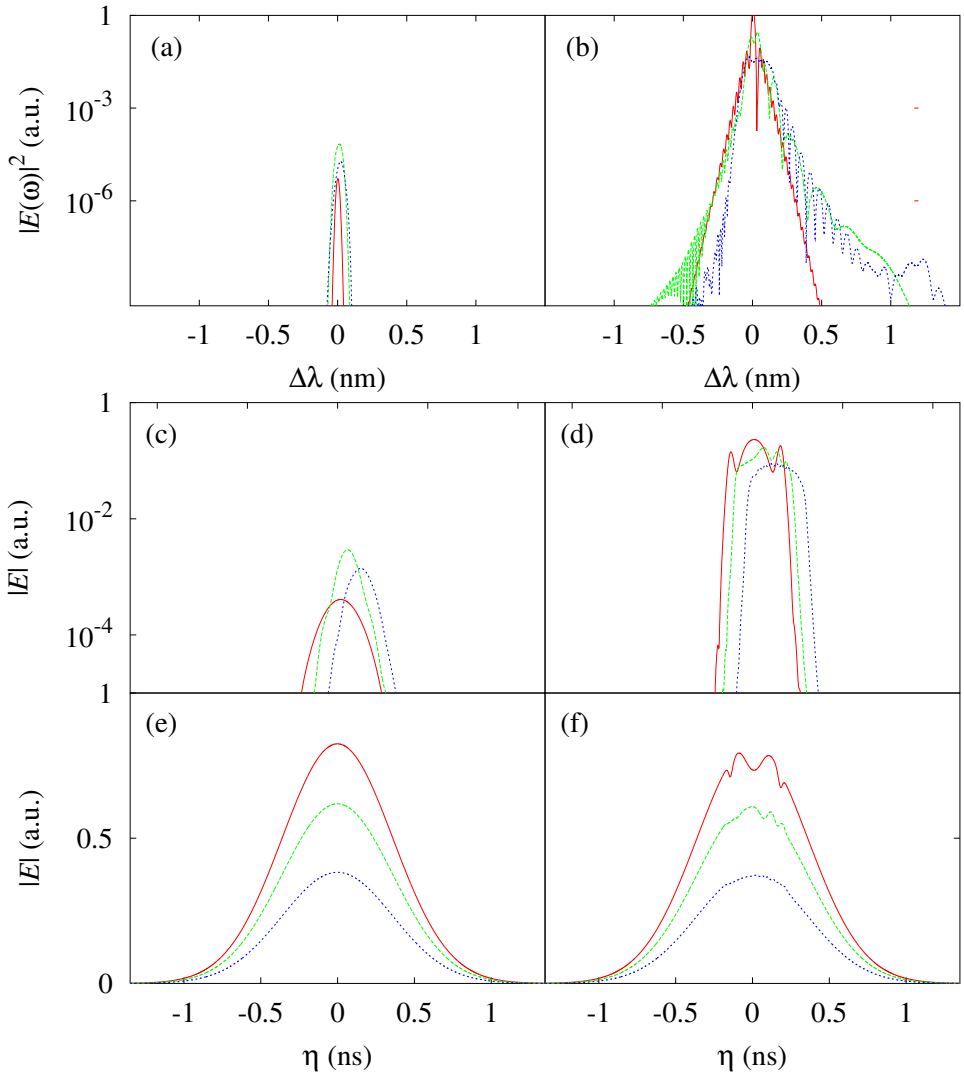

Figure 4.8: Spectral (a),(b) and temporal (c)-(f) shapes of idler (a)-(d) and pump (e),(f) pulses. Input pump intensity is 5.4×10^8 TW/cm^2 for (a),(c),(e) and 1.08×10^9 for (b),(d),(e). Propagation length is 10 m (red curves), 25 m (green curves) and 50 m (blue curves) in PCF with $\Lambda = 3.5$ μm, $d = 3.4$ μm.

to amplitude modulation instability experienced by the idler pulse in the anomalous dispersion regime.

4.3.3 Influence of birefringence

The possibility to create a narrow spectrum like the one shown in Fig. 4.8(a), as well as the dependence of idler wavelength on fiber geometry, raises the question: Is it possible to control the idler wavelength by the external influence, for example by introducing birefringence to the fiber? PCF's possessing birefringence were already proposed and produced by introducing holes of different diameter [90], changing the shape of the holes [91] and their positions [92]. It was shown that high values of birefringence [90] and polarization modulational instability [92] occur in such fibers. As such, the dependence of the phase-matching in the FWM on the birefringence was already studied in detail [93, 94], however the specific geometry of the PCFs allows especially large distance to the sidebands. The example how the external control of birefringence can be performed in PCF's is given in Ref. [95], where the polymer is introduced into two holes in the PCF cladding. By changing the temperature of the fiber, control over the refractive index of this polymer and thus over birefringence is achieved. For the description of birefringence it is necessary to use a model which does not rely on a weakly-guiding approximation. The assumption that the difference between the refractive indexes of the core $n_0 = n_{silica}$ and cladding $n_1 = n_{eff}$ is much smaller than unity does not hold, in the considered case it can be up to 0.5. Therefore, the expressions for the fields and the birefringence derived in Ref. [96] are used here. The equations are written in the nonorthogonal coordinates ρ and ϕ

related to the Cartesian coordinates by

$$x = a\rho\cos\phi \tag{4.8}$$

$$y = a\rho\sqrt{1-e^2}\sin\phi, \tag{4.9}$$

where $e = \sqrt{1-b^2/a^2}$ is the ellipticity, a and b denoting the major and minor semiaxis, respectively. After rewriting the Helmholtz equation in this coordinate system, the solution for the longitudinal components of the electric field E_z can be found for the two dominant modes, denoted by the superscripts a and b, in the fiber:

$$\begin{aligned} E_z^a &= AJ_1(u\rho)\cos\phi + \frac{1}{8}e^2 Au\rho J_2(u\rho)\cos\phi + \\ &\quad e^2\left[BJ_3(u\rho) + \frac{1}{8}Au\rho J_4(u\rho)\right]\cos 3\phi \end{aligned} \tag{4.10}$$

$$\begin{aligned} E_z^b &= AJ_1(u\rho)\sin\phi + \frac{3}{8}e^2 Au\rho J_2(u\rho)\sin\phi + \\ &\quad e^2\left[BJ_3(u\rho) + \frac{1}{8}Au\rho J_4(u\rho)\right]\sin 3\phi \end{aligned} \tag{4.11}$$

inside the core ($\rho < 1$) and

$$\begin{aligned} E_z^a &= CK_1(v\rho)\cos\phi + \frac{1}{8}e^2 Cv\rho K_2(v\rho)\cos\phi + \\ &\quad e^2\left[DK_3(v\rho) + \frac{1}{8}Cv\rho K_4(v\rho)\right]\cos 3\phi \end{aligned} \tag{4.12}$$

$$\begin{aligned} E_z^b &= CK_1(v\rho)\sin\phi + \frac{3}{8}e^2 Cv\rho K_2(v\rho)\sin\phi + \\ &\quad e^2\left[DK_3(v\rho) + \frac{1}{8}Cv\rho K_4(v\rho)\right]\sin 3\phi. \end{aligned} \tag{4.13}$$

Here u and v have the same meaning as in Chapter 2. Other components of the electric field as well as the magnetic field can be derived from the Maxwell equations. The resulting system of linear equations for A, B, C, D has a solution only if the determinant of the system equals zero. Wavenumbers of both

modes differ from the wavenumber h_0 obtained from the dispersion relation derived in Chapter 2 by the amount of the order of e^2. The birefringence is characterized by the difference of these wavenumbers $\Delta\beta = e^2 k_0 n_1 \Delta$, where

$$\Delta = \frac{1}{8k_0 n_1 h_0 a^2} \frac{V^2 + uv(uK - vJ) + X_3}{V^2 Y_3/(u^2 v^2) - X k_0^2 a^2/(2V^2)}. \tag{4.14}$$

In this expression, the following notations are used:

$$J = J_0(u)/J_1(u), \quad K = K_0(v)/K_1(v), \tag{4.15}$$

$$X_1 = uJ - 1, \quad Y_1 = -vK - 1, \tag{4.16}$$

$$X_2 = \frac{1 + J^2}{u^2} - \frac{2}{u^4}, \quad Y_2 = \frac{1 - K^2}{v^2} + \frac{2}{u^4}, \tag{4.17}$$

$$X_3 = (uJ + vK)(uJ - vK + uvJK), \quad Y_3 = 1 + 2h_o^2 a^2 \left(\frac{1}{u^2} - \frac{1}{v^2}\right) \tag{4.18}$$

$$X = (v^2 X_1 + u^2 Y_1)(n_0^2 X_2 + n_1^2 Y_2) + (n_o^2 v^2 X_1 + n_1^2 u^2 Y_1)(X_2 + Y_2). \tag{4.19}$$

The relation (4.14) was used to calculate the modification of the wavenumber for the idler and signal waves, which are assumed to have the polarization orthogonal to that of the pump wave. Due to different polarizations of the three waves, the system (4.6) is correspondingly modified [50]: the cross-phase modulation terms are multiplied by 2/3 and resonant terms are multiplied by 1/3. The values of the squared birefringence up to 0.35 are considered, although there can be deviations from the exact values of Δ for the higher birefringencies, since the theory used here is first-order in e^2. As shown in Fig. 4.9, changing birefringence allows to control the idler wavelength in the region where the dispersion of silica is small. With increasing intensity, the spectra will become broad, similar to Fig. 4.8, which can be undesirable. The model developed here can be thus used to predict the optimum pump intensity. The change caused by birefringence induces an almost linear shift of the idler wavelength over a large interval. The idler spectra shown in the

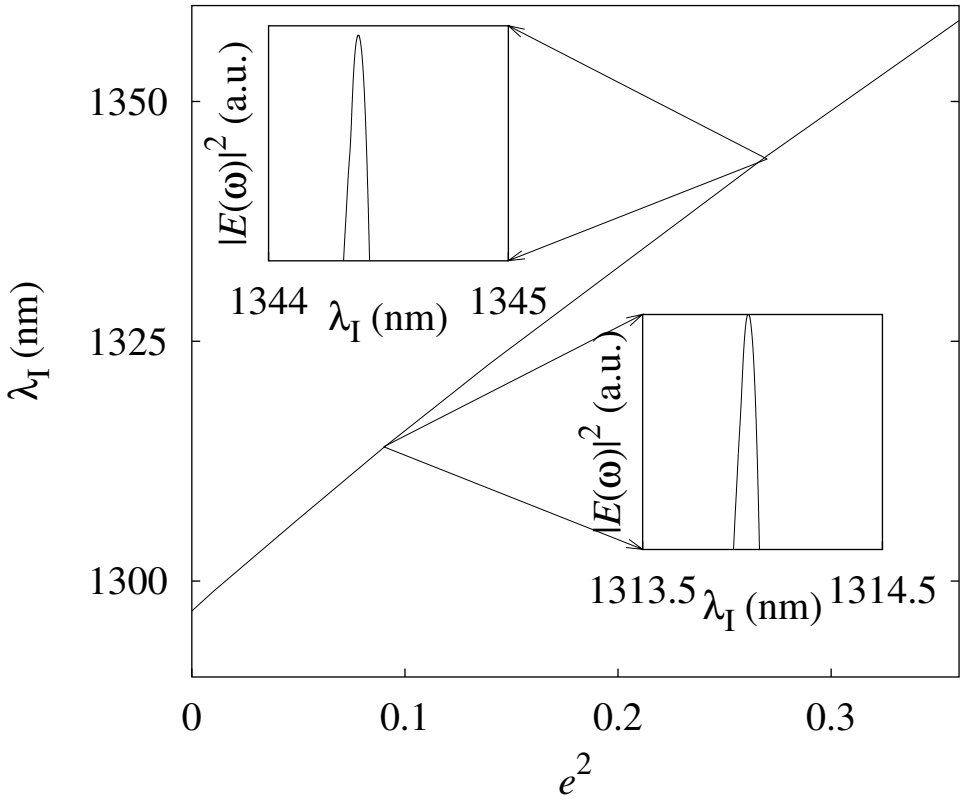

Figure 4.9: Idler wavelengths versus squared birefringence for a fiber with $\Lambda = 3.5$ μm, $d = 2.526$ μm. The insets show the spectrum of idler pulse after 25 m propagation for e^2 of 0.09 and 0.27, as shown by arrows. Vertical scale of the insets corresponds to 4 orders of magnitude

insets imply the generation of the spectrally narrow radiation, which can have important applications. For example, soliton propagation in this range can be achieved with a lower intensity. A system with an adjustable output wavelength can be also used for the needs of telecommunication.

Thus the change of birefringence of PCF's by external means can lead to a creation of a source which can be controlled over the low-loss window around the 1.3-μm wavelength.

In conclusion of this Chapter, the role of the 4-wave-mixing in generation of broadband radiation in PCF's was studied. The peculiarity of dispersion in PCF's results in the modified phase-matching condition, which predicts the generation of sidebands far from the pump frequency for PCF's and tapered fibers. It is shown that control over the positions of the sidebands can be achieved by changing the input intensity and frequency. To obtain effective phase-matching for the pump far in the normal dispersion regime, ps-duration pulses are necessary. For ps pulses necessary to obtain effective FWM with pump in the normal dispersion region, the process is studied by the application of a SVEA. The control of birefringence allows shifting the idler wavelengths in the range around 1.3 μm which is interesting for applications.